Theor. Comput. Fluid Dyn. (2011) 25:31–42
DOI 10.1007/s00162-009-0167-9

ORIGINAL ARTICLE

**X. Mao · S. J. Sherwin · H. M. Blackburn**

# Transient growth and bypass transition in stenotic flow with a physiological waveform

Received: 21 May 2009 / Accepted: 13 August 2009 / Published online: 23 October 2009


**Abstract** A direct analysis method is applied to compute optimal transient growth initial conditions for physiologically relevant pulsatile flows in a smooth axisymmetric stenosis with 75% occlusion. The flow waveform employed represents phase-average measurements obtained in the human common carotid artery. Floquet analysis shows that the periodic flow is stable to infinitesimal eigenmodal-type perturbations that would grow from one cycle to the next at the Reynolds numbers considered. However, the same flows display explosive transient growth of optimal disturbances, with our analysis predicting disturbance energy growths of order $10^{25}$ within half a pulse period at a mean bulk flow Reynolds number $Re = 300$, which is significantly lower than the physiological value of $Re = 450$ at this location. Direct numerical simulation at $Re = 300$ shows that when the base flow is perturbed a small amount with the optimal growth initial condition, the disturbance grows rapidly in time in agreement with the linear analysis, and saturates to provide a locally turbulent state within half a pulse period. This transition resulting from non-normal growth mechanisms shows the flow exhibits bypass transition to turbulence. Our analysis suggests that this route to localized turbulent states could be relatively common in human arterial flows.

**Keywords** Physiological flow · Transient growth · Stability · Global modes · Bypass transition

**PACS** 47.63.Cb · 47.15.Fe · 47.20.Ib · 47.27.Nf

## 1 Introduction

Laboratory and numerical studies of both steady and pulsatile flows in idealized stenotic constrictions (Fig. 1a) and bifurcations over the past four decades have been motivated by the desire to understand flow characteristics in the human physiology and their linkage to diseases of the arterial system. Flows in stenotic vessels are of particular interest owing to their association with atherosclerosis and thrombogenesis. With recent expansions in computational capacity and methods, particularly for flows in complex geometries, studies employing direct numerical simulation have begun to make a contribution to this area [3,12–14]. As had originally been suggested by the in vitro experiments [7,8], transition to turbulence has emerged as a common theme in studies of flows at Reynolds numbers relevant to the larger arteries of the human physiology.

Communicated by T. Colonius

X. Mao · S. J. Sherwin (✉)
Department of Aeronautics, Imperial College, Exhibition Road, SW7 2AZ London, UK
E-mail: s.sherwin@imperial.ac.uk

X. Mao
E-mail: x.mao07@imperial.ac.uk

H.M. Blackburn
Department of Mechanical and Aerospace Engineering, Monash University, 3800 Clayton,Victoria, Australia
E-mail: hugh.blackburn@eng.monash.edu.au

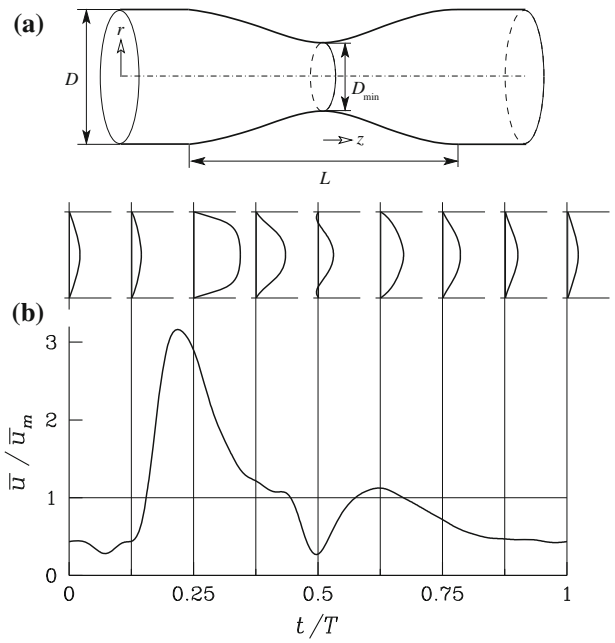


**Fig. 1** **a** Stenosis geometry and **b** Phase-averaged common carotid artery flow waveform, with velocity profiles for $Re = 400$

With the desire to understand factors underlying transition to turbulence, especially in idealized axisymmetric geometries, we have previously employed numerical asymptotic global stability analysis of both steady and pulsatile flows in an axisymmetric rigid tube with a smooth axisymmetric stenosis of 75% area occlusion [3,12]. In this work it was observed that the key features of the base flows in an asymmetric geometries are axisymmetric shear layers that separate from the wall just downstream of the stenosis throat, and vortex rings formed from roll-up of these shear layers when the flow is pulsatile. As would be expected, all the observed dynamics and instabilities are associated with these flow features. Asymptotic/long-time global stability analysis of pulsatile flows amounts to Floquet analysis, since base flows are time-periodic. Such analysis makes the assumption that instabilities grow by a constant multiplicative factor between successive pulses while retaining a mode shape specific to the phase point within the pulse cycle that is being studied. Our initial studies [3,12] involved idealized flow waveforms with at most two temporal Fourier harmonics and these suggested that as dimensionless pulse periods become longer (which is more relevant to the in-vivo conditions in larger arteries), flows become relatively more stable to Floquet-type instabilities.

More recently we have examined optimal transient growth initial conditions for both steady and pulsatile stenotic flows [5]. This analysis has highlighted that even if pulsatile flows are stable to Floquet-type global instabilities, extremely large ($O(10^{10})$ in study [5]) transient energy growth is possible for suitable initial disturbances within the time-span of a single pulse. The purpose of the present work is to examine the effect of using a more complex and physiologically realistic flow waveform on both long-time asymptotic/Floquet instabilities as well as transient growth analysis.

The outline of this paper is as follows: In Sect. 1.1 we define the geometric problem and flow conditions, in Sect. 2 we outline the numerical methods adopted in the analysis. In Sect. 3 we present the results of our direct stability analysis and direct numerical simulations. Finally in Sect. 4 we provide a brief discussion and summarize the findings of our study.

### 1.1 Problem description

We consider pulsatile flows of Newtonian fluid with kinematic viscosity $\nu$ in a rigid straight tube, diameter $D$, with a smooth axisymmetric constriction of co-sinusoidal shape as illustrated in Fig. 1a. The relative occlusion is $S = \frac{1-D_{\min}^2}{D^2}$. In our case, $D_{\min}/D = 0.5$, i.e. , $S = 0.75$, and the total length of the constriction considered is $L = 2D$. The same geometry has been chosen in a number of previous investigations, both in vitro and numerical.

**Table 1** Harmonic coefficients for phase-averaged pulsatile waveform $\bar{u}(t)/\bar{u}_m$ shown in Fig. 1b

| $n$ | $A_n$ | $B_n$ | $n$ | $A_n$ | $B_n$ | $n$ | $A_n$ | $B_n$ |
|---|---|---|---|---|---|---|---|---|
| 0 | 1 | 0 | 6 | −0.1041 | 0.1149 | 12 | −0.02045 | 0.03278 |
| 1 | −0.2264 | 0.591 | 7 | −0.03886 | 0.01257 | 13 | −0.01162 | 0.002044 |
| 2 | −0.6183 | 0.07234 | 8 | −0.06137 | −0.04677 | 14 | −0.01869 | −0.001022 |
| 3 | 0.04647 | −0.4058 | 9 | 0.05177 | −0.03975 | 15 | 0.0009446 | −0.01793 |
| 4 | 0.1555 | −0.1639 | 10 | 0.0136 | 0.0109 | 16 | 0.009188 | 0.001358 |
| 5 | 0.2239 | 0.1471 | 11 | 0.03434 | 0.02011 | | | |

Ratio of peak bulk flow rate to mean flow rate $\bar{u}_{\text{peak}}/\bar{u}_m = 3.17$

When considering a pulsatile and time periodic inflow, the space–time structure of the radial profile is described analytically as a sum of Bessel–Fourier components [11]. As in our previous work [12,3,5], these analytical solutions are used to supply inflow boundary conditions to the base flows. In summarizing the inflows, we employ the instantaneous area-average speed $\bar{u}$ and its time average $\bar{u}_m$:

$$\bar{u}(t) = \frac{8}{D^2}\int_0^{D/2} u(r,t)\, r\, \mathrm{d}r, \qquad \bar{u}_m = \frac{1}{T}\int_0^T \bar{u}(t)\, \mathrm{d}t,$$

where $u(r,t)$ is the (axial) velocity and where $T$ is the pulse period. We will use $D$ as a length scale and $\bar{u}_m$ as a velocity scale, hence the time scale is $D/\bar{u}_m$. In addition to the pulsatile wave form to be defined shortly, the key dimensionless parameters of any bulk-flow waveform are its time-average Reynolds number $Re = \bar{u}_m D/\nu$ and the reduced velocity $U_{\text{red}} = \bar{u}T/D$. The reduced velocity provides the number of tube diameters the mean flow travels in a pulse period, but alternatively may be considered as a dimensionless pulse period. In the following work we consider a pulsatile waveform shown in Fig. 1b which was obtained from ultrasound analysis of flow in a human carotid artery. The cross-sectionally averaged data have been phase-averaged and are represented by a Fourier expansion containing a mean and 16 harmonics such that

$$\frac{\bar{u}(t)}{\bar{u}_m} = \sum_{n=0}^{n=16} A_n \cos(2n\pi t/T) + B_n \sin(2n\pi t/T) \tag{1}$$

where $T = 27.7$ and the harmonic energy is provided in Table 1. The radially varying inlet flows are computed from Sexl–Womersley's solution [11,15] for fully developed periodic pulsatile laminar flow in a circular tube.

The relevant physiological parameters for the data shown in Fig. 1b and Table 1 were: pulse period $T = 0.862\,\text{s}$, mean lumen diameter $D = 7.48\,\text{mm}$, mean velocity $\bar{u}_m = 0.24\,\text{m/s}$. With an assumed Newtonian kinematic viscosity for blood of $\nu = 4\times10^{-6}\,\text{m}^2/\text{s}$, the Reynolds number $Re = 450$ while the reduced velocity $U_{\text{red}} = 27.7$. In the analysis to follow, we have kept the reduced velocity and bulk-flow waveform constant and used the Reynolds number as a variable parameter. In reality one would expect the Reynolds number, reduced velocity, and waveform all to be functions of physiological state. Note that with the peak/mean ratio of bulk flow rates of 3.17 for the chosen waveform (see Fig. 1b, Table 1), the effective peak systolic Reynolds number is 3.17 times larger than the mean value we use as a parameter.

## 2 Methodology

Assuming the fluid to be Newtonian and the flow incompressible, the relevant equations of motion for the primitive (velocity, pressure) variables are the incompressible Navier–Stokes equations

$$\partial_t \boldsymbol{u} = -\boldsymbol{u}\cdot\nabla\boldsymbol{u} - \nabla p + \nu\nabla^2\boldsymbol{u}, \text{ with } \nabla\cdot\boldsymbol{u} = 0, \tag{2}$$

where $\boldsymbol{u} = \boldsymbol{u}(z,r,\theta,t) = (u,v,w)(t)$ is the velocity field, $P = p/\rho$ is the modified pressure, and $\nu$ is the fluid's kinematic viscosity. The variables $z$, $r$, $\theta$, and $t$ are, respectively, the axial, radial, azimuthal, and time coordinates and $u$, $v$, $w$ the velocity components in the axial, radial, and azimuthal directions.

The methods employed to examine linear asymptotic stability or transient growth of disturbances are based on time integration of the linearized Navier–Stokes equations, which for a perturbation flow $\boldsymbol{u}'$ and kinematic pressure $p'$ in spatial domain $\Omega$ are

$$\partial_t \boldsymbol{u}' = -(\boldsymbol{U}\cdot\nabla)\boldsymbol{u}' - (\boldsymbol{u}'\cdot\nabla)\boldsymbol{U} - \nabla p' + Re^{-1}\nabla^2\boldsymbol{u}', \text{ with } \nabla\cdot\boldsymbol{u}' = 0 \quad \text{in } \Omega. \tag{3}$$

Their action on an initial perturbation $\boldsymbol{u}'(0)$ over time interval $\tau$ may be stated as $\boldsymbol{u}'(\tau) = \mathscr{A}(\tau)\boldsymbol{u}'(0)$; the asymptotic/large-time behavior of linear perturbations is exponential and governed by the leading eigenmodes of $\mathscr{A}(\tau)$. We note that in the present case the base flow is a $T$-periodic function of time, i.e. , $\boldsymbol{U}(t+T) = \boldsymbol{U}(t)$.

### 2.1 Linear asymptotic stability analysis

Through the eigensystem decomposition of this forward evolution operator $\mathscr{A}(\tau)$ we may determine the asymptotic stability of the base flow $\boldsymbol{U}$. In this case the solution is proposed to be the sum of eigenmodes, $\boldsymbol{u}'(\boldsymbol{x}, t) = \sum_j \exp(\lambda_j t)\tilde{\boldsymbol{u}}_j(\boldsymbol{x}) + \text{c.c.}$, and we examine the eigenvalue problem

$$\mathscr{A}(\tau)\tilde{\boldsymbol{u}}_j = \mu_j \tilde{\boldsymbol{u}}_j, \quad \mu_j \equiv \exp(\lambda_j \tau). \tag{4}$$

If $\boldsymbol{U}$ is steady, then the largest eigenvalues $\mu_j$ of $\mathscr{A}(\tau)$ map to the eigenvalues $\lambda_j$ of largest real part for linear system (3), while the eigenmodes of $\mathscr{A}(\tau)$ and those of (3) are the same. If $\boldsymbol{U}$ is $T$-periodic then we set $\tau = T$ and consider this as a temporal Floquet problem, in which case the $\mu_i$ are Floquet multipliers and the eigenmodes of $\mathscr{A}(\tau)$ are the $T$-periodic Floquet modes $\tilde{\boldsymbol{u}}_j(\boldsymbol{x}, t+T) = \tilde{\boldsymbol{u}}_j(\boldsymbol{x}, t)$ evaluated at a specific temporal phase. Asymptotic instability of both steady and simple pulsatile stenotic flows (corresponding to $|\mu_j| > 1$) in the present problem was dealt with by [3] and [12]. In the following we address transient growth over finite times.

### 2.2 Optimal transient growth analysis

Where asymptotic instability is concerned with energy growth of perturbations in the long-time-limit, optimal transient growth is concerned with the maximum energy growth for all possible initial perturbations over a finite time interval. We take a direct approach to computing initial conditions that lead to optimal transient growth, as described in [1,4,5]. As is typical [10] we define transient growth with respect to the energy norm of the perturbation flow, derived from the $L_2$ inner product

$$2E(\boldsymbol{u}') = (\boldsymbol{u}', \boldsymbol{u}') \equiv \int_\Omega \boldsymbol{u}' \cdot \boldsymbol{u}' \, \mathrm{d}V,$$

where $E$ is the kinetic energy per unit mass of a perturbation, integrated over the full domain. If the initial perturbation $\boldsymbol{u}'(0)$ is taken to have unit norm, then the transient energy growth over interval $\tau$ is

$$E(\tau)/E(0) = \big(\boldsymbol{u}'(\tau), \boldsymbol{u}'(\tau)\big) = \big(\mathscr{A}(\tau)\boldsymbol{u}'(0), \mathscr{A}(\tau)\boldsymbol{u}'(0)\big) = \big(\boldsymbol{u}'(0), \mathscr{A}^*(\tau)\mathscr{A}(\tau)\boldsymbol{u}'(0)\big),$$

where we introduce $\mathscr{A}^*(\tau)$, the adjoint of the forward evolution operator $\mathscr{A}(\tau)$. The action of $\mathscr{A}^*(\tau)$ is obtained by integrating the adjoint linearized Navier–Stokes equations

$$-\partial_t \boldsymbol{u}^* = -(\boldsymbol{U}\cdot\nabla)\boldsymbol{u}^* + (\nabla \boldsymbol{U})^{\mathrm{T}} \cdot \boldsymbol{u}^* - \nabla p^* + Re^{-1}\nabla^2 \boldsymbol{u}^*, \ \text{with } \nabla \cdot \boldsymbol{u}^* = 0 \ \text{ in } \Omega \tag{5}$$

backwards over interval $\tau$. $\mathscr{A}(\tau)$ evolves the initial perturbations forward as $\boldsymbol{u}'(\tau) = \mathscr{A}(\tau)\boldsymbol{u}'(0)$ while the adjoint operator $\mathscr{A}^*(\tau)$ evolves the perturbation backwards as $\boldsymbol{u}'(0) = \mathscr{A}^*(\tau)\boldsymbol{u}'(\tau)$. Comparing systems (3) and (5) we observe that in the adjoint system the $\partial_t$ and $(\boldsymbol{U}\cdot\nabla)\boldsymbol{u}^*$ terms negated. The sign on the $\partial_t$ term implies that the adjoint system is only well-posed in the negative time direction. The action of the symmetric operator $\mathscr{A}^*(\tau)\mathscr{A}(\tau)$ on $\boldsymbol{u}'$ is obtained by sequential time integration of $\mathscr{A}(\tau)$ and $\mathscr{A}^*(\tau)$, i.e. , first use $\boldsymbol{u}'(0)$ to initialize the integration of (3) forwards in time over interval $\tau$, then use the outcome to initialize the integration of (5) backwards in time over the same interval.

The optimal perturbation (leading to largest energy growth over $\tau$) is the eigenfunction of $\mathscr{A}^*(\tau)\mathscr{A}(\tau)$ corresponding to the joint operator's dominant eigenvalue, and so we seek the dominant eigenvalues $\lambda_j$ and eigenmodes $\boldsymbol{v}_j$ of the problem

$$\mathscr{A}^*(\tau)\mathscr{A}(\tau)\boldsymbol{v}_j = \lambda_j \boldsymbol{v}_j.$$

Typically $G(\tau) = \max(\lambda_j)$ is used to denote the maximum energy growth obtainable at time $\tau$, while the global maximum is denoted by $G_{\max} = \max_\tau G(\tau)$. On the other hand, $\boldsymbol{v}_j$ corresponding to $G(\tau)$ denotes the

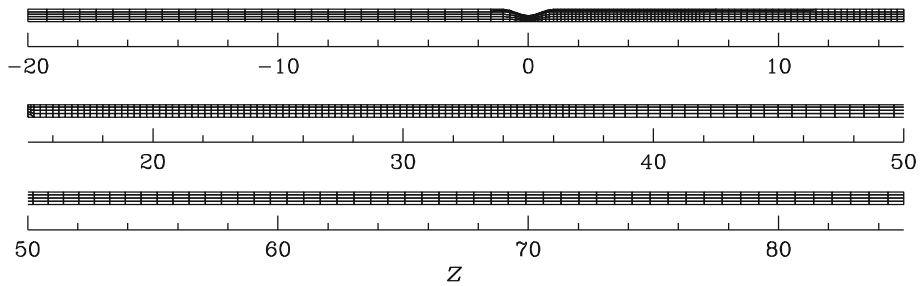


**Fig. 2** Computational mesh in the meridional semi-plane for a cylindrical-coordinate discretization of the geometry, with 1336 spectral elements. Overall domain length $105D$

optimal initial perturbation that leads to the optimal growth. An Arnoldi method is adopted to calculate the maximum eigenvalues and corresponding eigenvectors of the joint matrix $\mathscr{A}^*(\tau)\mathscr{A}(\tau)$.

We note that the eigenfunctions $\boldsymbol{v}_j$ correspond to right singular vectors of operator $\mathscr{A}(\tau)$, while their ($L_2$-normalized) outcomes $\boldsymbol{u}_j$ under the action of $\mathscr{A}(\tau)$ are the left singular vectors, i.e.,

$$\mathscr{A}(\tau)\boldsymbol{v}_j = \sigma_j \boldsymbol{u}_j, \tag{6}$$

where the sets of vectors $\boldsymbol{u}_j$, $\boldsymbol{v}_j$ are each orthonormal, and where $\sigma_j^2 = \lambda_j$. The singular values of $\mathscr{A}(\tau)$ are $\sigma_j = \lambda_j^{1/2}$, where both $\sigma_j$ and $\lambda_j$ are real and non-negative.

While long-time asymptotic growth is determined from the eigensystem of $\mathscr{A}(\tau)$, optimal transient growth is described in terms of the singular value decomposition (6): the optimal initial condition and its (normalized) outcome after evolution over time $\tau$ are, respectively, the right and left singular vectors of the forward operator $\mathscr{A}(\tau)$ corresponding to the largest singular value, whose square (the largest eigenvalue of $\mathscr{A}^*\mathscr{A}$) is the optimal energy growth $G(\tau)$.

When a base flow is non-steady, an additional parameter enters into transient growth analysis, which is the time at which a perturbation is initiated relative to the base flow time-base. When the base flow is $T$-periodic, this parameter can be described by the phase-point $t_0/T$, and is readily incorporated into the analysis by time-shifting the base flow by $t_0$. For an open flow, the most straightforward perturbation velocity boundary condition to apply on both the inflow and outflow (and at solid walls) are homogeneous Dirichlet, i.e. , $\boldsymbol{u}' = \boldsymbol{0}$ over the whole boundary for both the forward and adjoint linearized Navier–Stokes equations. Further discussion of our choice of boundary conditions, methodology and implementation of transient growth analysis for non-parallel shear flows both steady and $T$-periodic is provided in [1,4,5].

## 2.3 Discretization

Spectral elements are used for spatial discretization of the axisymmetric geometry in the meridional semi-plane, coupled with a Fourier decomposition in azimuth. Details of the discretization and its convergence properties are given in [2]. Time integration is carried out using a second-order velocity-correction scheme. The same numerics are used to compute base flows and the actions of the forward and adjoint linearized Navier–Stokes operators, with the same time-step being retained for all three integrations. As discussed in [3], long domains are required for the numerical linear stability analysis of these flows; the same is true for transient growth analysis, especially when the flow is pulsatile and the reduced velocity is large. Figure 2 shows the computational mesh used for the present analysis, where it can be seen that the inflow and outflow lengths relative to the throat of the stenosis are, respectively, 20 and 85 $D$. Mesh structure near the throat is similar to that in [3]. In the present problem, a high peak velocity, fine mesh structure where velocity is at its largest, and comparatively large Reynolds numbers have meant that CFL-type stability restrictions demanded a comparatively small time-step: we have used 204 800 time steps per pulse period for computing all results.

The $T$-periodic base flows are pre-computed as axisymmetric solutions of the Navier–Stokes equations (2) and stored as data for the transient growth analysis. At any phase point in the pulse cycle, the base flow is then reconstructed from these stored time slices. Owing to the non-trivial structure of the bulk flow waveform and the resulting jet downstream of the stenosis in the present problem, very rapid temporal variation of base flow velocity can occur at some spatial locations, requiring a comparatively large number of time slices of the base

**Table 2** Convergence data for $t_0/T = 0$, $\tau/T = 0.5$, $Re = 300$, $k = 1$

| Polynomial order $n$ | 4 | 5 | 6 | 7 |
|---|---|---|---|---|
| Maximum energy growth $G$ | $1.03 \times 10^{25}$ | $1.13 \times 10^{25}$ | $1.13 \times 10^{25}$ | $1.13 \times 10^{25}$ |
| % difference | 8.8 | 0.0 | 0.0 | – |

$n$ is the polynomial order used to provide tensor-product shape functions in each spectral element and $G$ is the energy growth attained by the computed initial condition at $\tau/T = 0.5$

flow to be retained for this reconstruction. The timescale of these temporal fluctuations reduces with increasing Reynolds number, requiring a greater number of time slices to be retained at high Reynolds numbers. For the computations reported here, 512 time slices were used as this was shown adequate for Reynolds numbers up to $Re = 400$, the maximum value considered. We note that the need for this reconstruction is partly forced by the nature of the transient growth iteration, which requires backward time integration to compute the action of $\mathscr{A}^*$. For the forward integration required to compute the action of $\mathscr{A}$, the base flow could be integrated forwards (concurrently if desired) so that reconstruction could be avoided if required. However, the Navier–Stokes equations used to compute the base flow cannot be stably integrated backward in time owing to the influence of viscous diffusion.

With such a large number of time slices, reconstruction of the base flow becomes the dominant work component in time-stepping if Fourier reconstruction is used, which has been our practice in past work. In order to overcome this difficulty we investigated both cubic spline reconstruction based on all time slices and local four-point-Lagrange (i.e. , local cubic) reconstruction. The work involved in global cubic spline interpolation is similar to that for Fourier reconstruction, but local cubic interpolation is much cheaper while delivering formally the same order of accuracy. With 512 time slices, the three methods deliver similar results in terms of base flow reconstruction, Floquet multipliers $\mu$ and optimal growth $G$ up to $Re = 400$, hence four-point Lagrange interpolation was adopted. For convenience and speed all the base flow data were retained in core memory but only four slices are actually needed in core to compute the interpolant at any instant so the majority could be kept in slower memory if required.

Since the flows are necessarily periodic in the azimuthal direction, Fourier projections are used for the azimuthal discretization. For stability and transient growth analysis, linearity ensures that each Fourier mode can be considered independently. The modal structure of the velocity and pressure perturbation fields is then (with $z$, $r$, and $\theta$, respectively, the axial, radial, and azimuthal coordinates, and $k$ as the azimuthal wavenumber)

$$u_z(z,r,\theta) = \hat{u}_z^k(z,r)\cos k\theta, \;\; u_r(z,r,\theta) = \hat{u}_r^k(z,r)\cos k\theta,$$
$$u_\theta(z,r,\theta) = \hat{u}_\theta^k(z,r)\sin k\theta, \;\; p(z,r,\theta) = \hat{p}^k(z,r)\cos k\theta,$$

(or their $\theta$-conjugates) since these shapes are invariant under the actions of (3) and (5).

A study of spatial convergence of optimum growth values approximating the global optimum for $Re = 300$ is presented in Table 2. This shows that to three significant figures there is no effect of increasing tensor-product polynomial order above $n = 5$. We have used $n = 6$ for the results reported in the following sections.

## 3 Results

Linear stability analysis and transient growth results are supplied in Sects. 3.2 and 3.3 for azimuthal wavenumber $k = 1$, which exploratory analysis has shown to host greatest amplification in both cases. The largest transient growth is also found to occur for a $k = 1$ azimuthal wavenumber for Poiseuille pipe flow [9] and for both steady and simple pulsatile flow at the lower reduced velocity of $U_{\text{red}} = 10$ in the present geometry [5]. Prior to presenting these results we briefly examine base flow vorticity in Sect. 3.1, and subsequently in Sect. 3.4 we present nonlinear (direct numerical simulation) results which demonstrate that transient growth leads to bypass transition for $Re = 300$.

### 3.1 Base flows

The nature of the pulsatile axisymmetric base flows is illustrated for $Re = 300$ by contours of azimuthal vorticity at eight phase points in Fig. 3. These phase points are consistent with the inflow profiles shown in Fig. 1b where the bulk flow profile in time is also shown. There are effectively two ejections per pulse cycle.

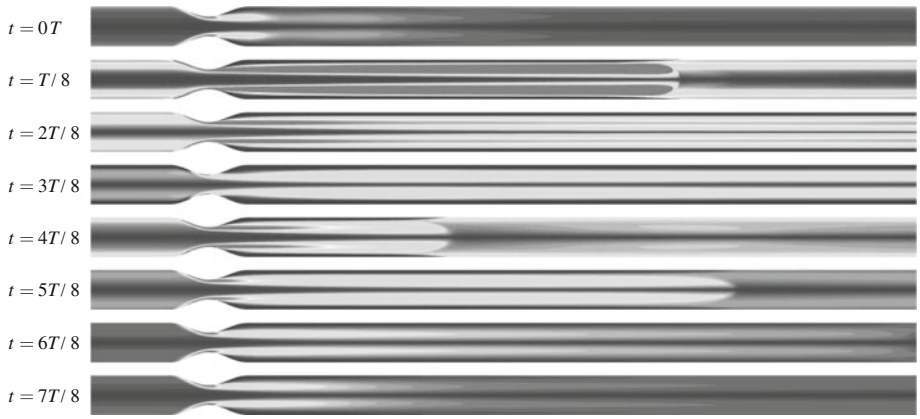


**Fig. 3** Contours of azimuthal vorticity in base flow for $Re = 300$, projected to a meridional plane over a range $-3D \leq z \leq 18D$ centered on the stenosis throat. Note that the computational domain has a much greater axial extent than shown here (see Fig. 2)

**Table 3** Asymptotic stability analysis

| $Re$ | 100 | 200 | 300 | 400 |
|---|---|---|---|---|
| $\mu$ | $-2.87 \times 10^{-9}$ | $-5.27 \times 10^{-7}$ | $-3.71 \times 10^{-3}$ | $-2.44 \times 10^{-1}$ |

Floquet multipliers for azimuthal wavenumber $k = 1$

Each ejection leads to the formation of a vortex ring followed by long shear layers. The primary ejection with a leading vortex ring is evident in Fig. 3 at $t = T/8$ while the secondary pulse and its associated vortex ring are evident at $t = 4T/8$ and $t = 5T/8$.

### 3.2 Floquet analysis: asymptotic stability

Floquet analysis was carried out over a range of Reynolds number up to $Re = 400$, and for this range the flow is observed to be linearly asymptotically stable. The leading Floquet multipliers are shown in Table 3 where we recall that a magnitude less than one indicates stability. The negative values of the Floquet multiplier indicate that they would lead to a period-doubling instability, just as we found at moderate Reynolds numbers in earlier work [3,12]— the period doubling is associated with alternate tilting of the vortex ring structures from one pulse period to the next. Therefore the conclusion that can be drawn from this analysis is that the flow is linearly asymptotically stable for $Re \leqslant 400$. Possibly the flow is linearly stable for Reynolds numbers somewhat above the physiological value of $Re = 450$. However our subsequent transient growth analysis is for $Re \leqslant 300$, when the flow definitely possesses asymptotic stability.

### 3.3 Linear optimal growth

The maximum Reynolds number we have considered for transient growth analysis is $Re = 300$. First, we confirm that as for the related flows previously studied, the largest growth again occurs in the $k = 1$ azimuthal wavenumber, as shown in Fig. 4. Axisymmetric disturbances ($k = 0$) are only marginally amplified at early times, while at most times they are strongly attenuated. Our subsequent linear analyses are confined to $k = 1$.

Figure 5 shows the envelopes of optimal growth for time intervals within a single pulse period and for four starting phases $t_0/T = 0$, 0.25, 0.5, and 0.75 (recall that $t_0/T = 0.25$ corresponds to initiation approximately in phase with peak flow, see Fig. 1b). As can be seen from this figure the largest observed growth in energy $G = 1.13 \times 10^{25}$ occurs at $\tau/T = 0.5$ and for $t_0/T = 0$.

For this flow the optimal transient growth values are, like the Floquet multipliers (Table 3), very sensitive to changes in Reynolds number. To illustrate this we show in Fig. 6 the envelopes of maximum transient growth at $Re = 200$ and 300, both for $t_0/T = 0$. Peak growth values increase by approximately 17 orders of magnitude as a result of increasing Reynolds number by factor of 1.5, however, the shapes of the transient growth envelopes are qualitatively similar at $Re = 200$ and 300, implying similar dynamics at both Reynolds numbers. For $Re = 100$, there is only small growth at early times: for most values of $t/T$ represented in Fig. 6,

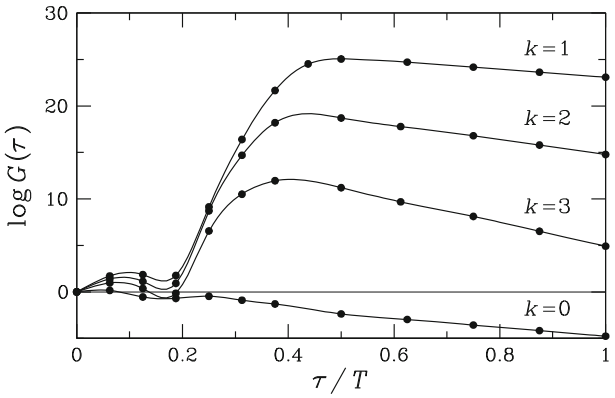


**Fig. 4** Optimal growth envelopes for disturbances in azimuthal wavenumbers $k = 0$–3, computed at $Re = 300$, perturbation initiation phase $t_0/T = 0$ relative to the base flow

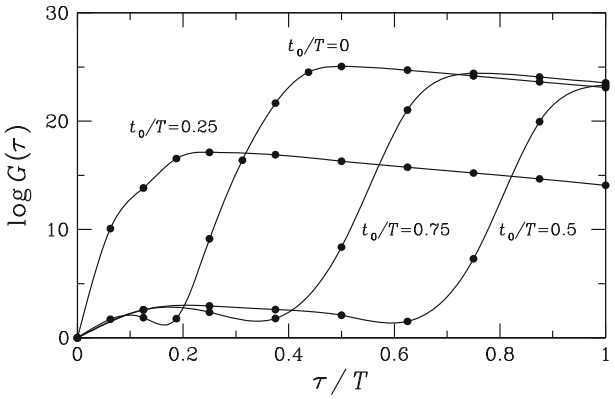


**Fig. 5** Optimal growth envelopes for disturbances in azimuthal wavenumber $k = 1$, computed at $Re = 300$, with different perturbation initiation phases $t_0/T$ relative to the base flow. Initiation at $t_0/T = 0.25$ corresponds approximately to perturbation in phase with systolic/peak flow (refer Fig. 1)

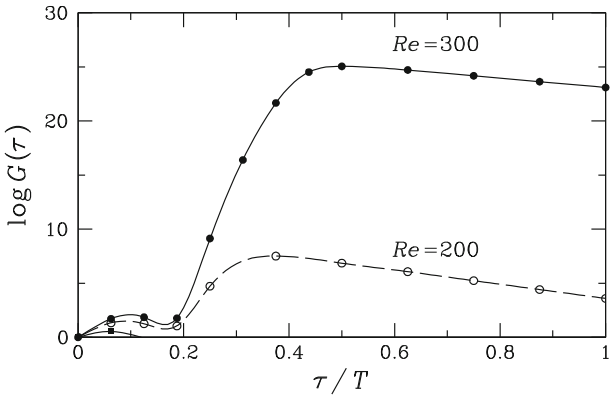


**Fig. 6** Optimal growth envelopes for disturbances in azimuthal wavenumber $k = 1$, computed at $Re = 200$ and 300, and initiated in phase with the (arbitrary) base flow phase reference point, i.e. , $t_0 = 0$. Data for $Re = 100$ are also represented, but result in only small growth at short evolution intervals ($t/T \sim 0.05$), and decay at larger intervals

there is substantial decay in energy. While we have not here examined in detail the dependence of peak energy growth on Reynolds number, we note that in a number of related (albeit steady) separated flows [4–6], peak energy growth is observed to increase exponentially with Reynolds number, as opposed to the $Re^2$ dependence typical of parallel shear flows.

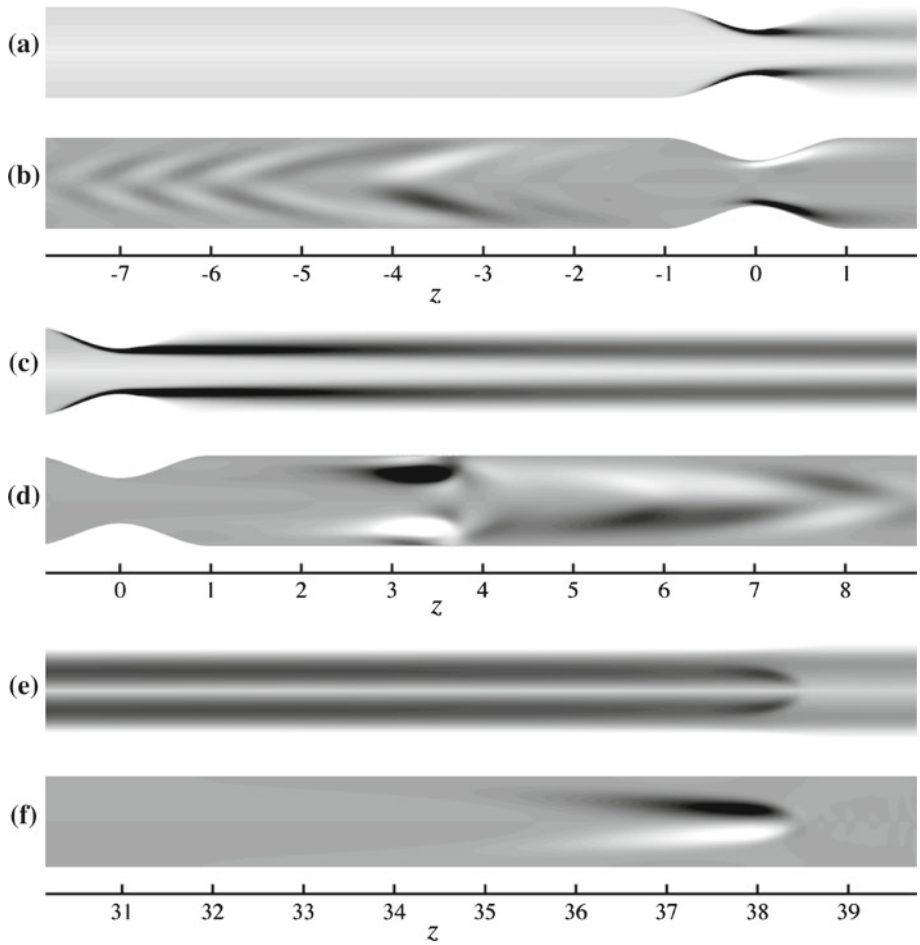


**Fig. 7** Initial condition and outcome for the most-amplified case at $Re = 300$, $t_0/T = 0$, $\tau/T = 0.5$, $k = 1$. **a, b** contours of base flow vorticity and perturbation axial velocity (white, positive; black, negative) for the initial condition; **c, d** during evolution, at $t/T = 0.390625$; **e, f** outcome at $t/T = 0.5$

Figure 7 shows the structure of the base flow and perturbation for the most-amplified case examined ($Re = 300$, $t_0/T = 0$, $\tau/T = 0.5$, $k = 1$) at initiation, $t/T = 0$, and at end of the time interval for maximum growth, $t/T = 0.5$. The base flow at initial time $t/T = 0.0$ and at time $t/T = 0.5$ corresponds to the views shown in Fig. 3 for $t = 0\,T$ and $t = 4T/8$ but we note that the leading edge of the first front (near $z = 38$) in Fig. 7c lies outside the field of view in Fig. 3.

The initial perturbation shown in Fig. 7b has two sets of features with similarities to those that we have previously observed (see Fig.7c, e in [5]). First, upstream of the stenosis, there is a set of chevron-shaped contours which corresponds to a sinuous disturbance to the flow about to be ejected through the throat. Second, there is a concentrated disturbance lying at the separation zone in the throat (near $z = 0$) — this latter feature, while superficially similar to the most-amplified initial disturbance shown in Fig. 7c of [5], differs in that it lacks a streamwise waviness since it involves only a perturbation of single sign in either the top or bottom half of the pipe. The perturbation at time for maximum growth, Fig. 7f has a simple structure that resides within the vortex ring that leads the pulsatile flow, near $z = 38$. The perturbation flow would lead to a counter-clockwise tilting of the vortex ring and we note that this mechanism and indeed the shape of the perturbation are very similar to what we have previously observed as a period-doubling Floquet mode in Fig. 16d, e, [12]. At an intermediate time point, $t/T = 0.390625$, between the initial and final state we observe the axial perturbation shown in Fig. 7d. In this figure we observe that both the chevron pattern associated with the initial perturbation upstream of the throat as well as the more concentrated structure initially arising at the throat are present. Interestingly, at this time point the chevron pattern has overtaken the concentrated perturbation. We have examined the progression of the perturbation at intermediate times, and see these two mechanisms at work throughout the

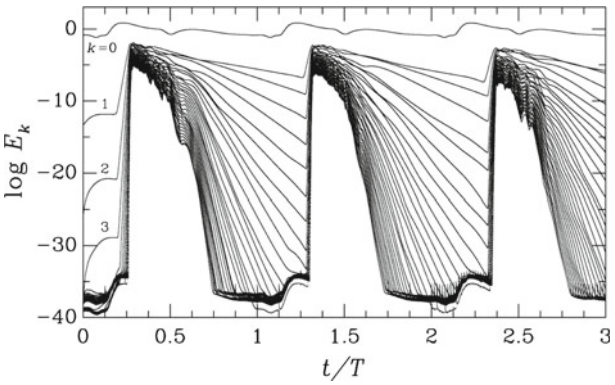


**Fig. 8** Time series of energies $E_k$ in azimuthal Fourier modes from a direct numerical simulation study at $Re = 300$ where the initial condition was seeded with the optimal disturbance at a relative energy level of $10^{-12}$

growth period. It appears that the chevron/sinuous disturbance in the extended shear layer of the base flow travels faster than the concentrated pattern as highlighted in Fig. 7d. However it is the concentrated pattern which creates an overturning-type perturbation to the leading base flow vortex ring that ultimately dominates, as shown in Fig. 7f.

### 3.4 Nonlinear analysis: bypass transition

Finally we turn to an examination of nonlinear behavior at $Re = 300$, which is computed with 32 azimuthal Fourier modes (i.e. , 64 planes of data in azimuth). The initial condition is a linear combination of the limit-cycle base flow and the optimal initial perturbation in azimuthal wavenumber $k = 1$, at a relative energy level of $10^{-12}$, so that the relative velocity scale of the perturbation is approximately six orders of magnitude smaller than that of the base flow, a relative size that would be undetectable in a physical experiment. We note that with a predicted linear transient growth of $1.13 \times 10^{25}$, the perturbation would reach an energy level well above that of the base flow for this ratio of initial energies. The initial state is then evolved over three pulse cycles via direct numerical simulation (DNS).

Figure 8 shows time series of energy in the Fourier modes contained in the simulation. The axisymmetric component corresponds to $k = 0$; the initial perturbation resides in $k = 1$, but rapidly spreads to all modes via nonlinearity. The low-level energy plateau at energies of order $10^{-38}$ corresponds to machine noise level. Perturbation energy grows comparatively slow at first, until shortly before $t/T = 0.25$, when it commences rapid exponential growth, reaching saturation soon after $t/T = 0.25$. The higher Fourier modes also grow rapidly, reaching a spread of approximately three orders of magnitude at saturation. We note that the qualitative form of the $k = 1$ mode in these non-linear simulations is similar to the linear transient growth mode in Fig. 5.

The nature of the flow near the time of initial saturation is illustrated in Fig. 9. At the pulse front there is initially (at $t/T = 0.281$) a strongly three-dimensional breakdown of the leading vortex ring, leading to a turbulent burst at the three later times. The flow between the breakdown and the stenosis is much closer to being axisymmetric. It is interesting to note that the axial location of the breakdown is approximately 15 diameters downstream of the throat, i.e. , well upstream of the location of the linear perturbation at the phase for maximum growth, which, as shown in Fig. 7d, is close to 38 diameters downstream of the throat. This difference is a consequence of the fact that the nonlinear growth saturates much earlier than the linear growth reaches a maximum. This evolution clearly demonstrates that transition to turbulence can be induced within a single pulse cycle when a trace amount of the optimal growth initial condition is added to the base flow. Since the transition does not occur through the standard eigenmodal mechanism (here, Floquet instability) but is driven by non-normal growth we may describe this as bypass transition [10].

Now returning to consideration of Fig. 8, we see that following the initial saturation, energy in all non-axisymmetric modes decreases, and for times $t/T > 0.75$ the decay of all these modes is approximately exponential. The energy in mode $k = 1$ decays to a level of order $10^{-7}$ and the spatial location of the majority of the associated energy will be well downstream of the throat. However, at $t/T \sim 1.25$, energy in all the non-axisymmetric modes again commences rapid exponential growth as the base flow pulse downstream of the stenosis reaches high velocity, and all the higher modes again follow this growth to another saturation shortly

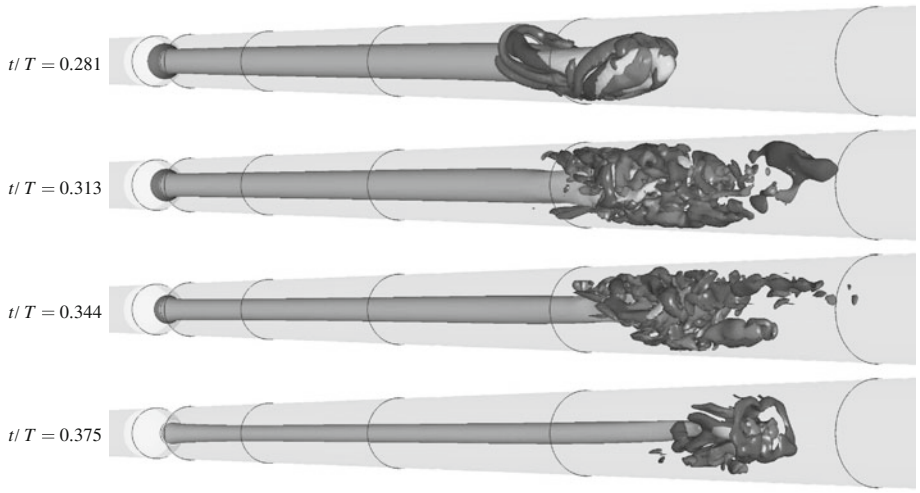


**Fig. 9** Perspective views of DNS results at four instants in the first pulse cycle after initiation in Fig. 8, using isosurfaces of (light grey) axial velocity and (mid/dark grey) radial velocity. The axial location of the pulse front and associated turbulent burst is approximately 15–20 pipe diameters downstream of the stenosis throat during this breakdown event

following this time. The behavior subsequently is superficially similar to that following the initial cycle, and the same pattern is repeated in the third cycle. On more detailed examination, we note that the peak energy associated with the turbulent burst declines slightly from cycle to cycle, while the phase at which transition occurs increases. These two effects are associated with the transition location moving downstream (of order 5 diameters) from one pulse to the next. Thus it appears that in the absence of further disturbance, the turbulence will eventually disappear at this Reynolds number. However, since the initial disturbance required to produce transition is vanishingly small, we would anticipate that in any physical experiment, where some degree of noise is always present, turbulence resulting from non-normal growth would be sustained.

## 4 Discussion and conclusions

As we have already noted some of the instability characteristics of this pulsatile flow in a 75% stenosis have been observed in our previous work. There are however also some notable differences.

First we note that in [3,12] a vortex ring tilting mechanism due to a $k = 1$ azimuthal perturbation was identified as an asymptotic Floquet instability at much lower reduced velocities ($2.5 < U_{\mathrm{red}}$). The low reduced velocity vortex tilting mechanism was a period-doubling-type mode associated with the vortices tilted from different pulses having opposite directions. However as the reduced velocity increases, a Floquet-type period-doubling instability becomes increasingly difficult to excite owing to increasing separation of pulse fronts, as we alluded to in [3]. Nevertheless, in place of this in the present flow, we have explosive transient growth involving a vortex-ring-tilting mechanism initiated by a combination of a shear layer instability and a concentrated perturbation at the throat of the stenosis. This instability is also most energetic when considering a $k = 1$ azimuthal mode.

At a reduced velocity of $U_{\mathrm{red}} \approx 10$ in [5] it was observed that significant growth $O(10^{10})$ was possible, owing to linear transient growth corresponding to a Kelvin–Helmholtz instability in the shear layer behind the vortex ring. The current study of a physiological pulsatile waveform highlights that a combination of the two previous types of instabilities, i.e. , vortex tilting instability and a transient shear layer instability, can lead to a transient instability mechanism with a growth of even larger magnitude.

Third, and possibly most significantly, through direct numerical simulation we have also observed a new feature of bypass transition associated with extremely large linear transient growth. Out of all the types of instability that we have considered, both asymptotic and transient, the transient growth vortex-ring-tilting mode initiated by a shear layer instability would appear to be the most likely to arise in vivo. This is because this transient instability has significant amplification at a realistic value of the non-dimensional pulse period (i.e. , $4T\bar{u}/D \approx 27.7$) and arises at physiologically relevant Reynolds numbers ($200 \leq Re \leq 400$).

Clearly, anatomically accurate geometry is another feature which is likely to play a role in a specific in vivo problem. In relation to this, we would highlight that in the present idealized geometry, the most unstable

perturbations are energized in the $k = 1$ azimuthal mode. This mode is likely to receive excitation in the presence of curvature, as shown by the Dean flow solutions of steady flow in a toroidal pipe. At present we are unable to offer definitive comment on the role of stenosis morphology but believe that shear layer instabilities and vortex tilting are likely to arise even if the stenosis is eccentric, providing the stenosis shape is such that it generates a vortex ring at its throat. It is also likely that a higher stenosis degree will make the flow more sensitive to this type of instability, and therefore bypass transition, as if all other conditions are kept the same and the stenosis degree is increased, the shear layer intensity will be enhanced, through increase in the throat Reynolds number. We would finally note that the transient growth analysis is applicable to any three-dimensional geometry providing a base flow can be identified, since any noise-free base state, symmetric or otherwise, provides an appropriate starting point.

**Acknowledgements** We would like to thank Professor Kim Parker of Imperial College London for providing the phase-average carotid artery flow waveform. We wish to acknowledge the support of Australia's National Computational Infrastructure Merit Allocation Scheme project D77. X. Mao would like to acknowledge the Student Opportunity Fund at Imperial College for financial support while S. J. Sherwin wishes also to acknowledge financial support from an EPSRC Advanced Research Fellowship.

## References

1. Barkley, D., Blackburn, H.M., Sherwin, S.J.: Direct optimal growth analysis for timesteppers. Int. J. Num. Meth. Fluids **57**, 1437–1458 (2008)
2. Blackburn, H.M., Sherwin, S.J.: Formulation of a Galerkin spectral element–Fourier method for three-dimensional incompressible flows in cylindrical geometries. J. Comput. Phys. **197**(2), 759–778 (2004)
3. Blackburn, H.M., Sherwin, S.J.: Instability modes and transition of pulsatile stenotic flow: pulse-period dependence. J. Fluid Mech. **573**, 57–88 (2007)
4. Blackburn, H.M., Barkley, D., Sherwin, S.J.: Convective instability and transient growth in flow over a backward-facing step. J. Fluid Mech. **603**, 271–304 (2008)
5. Blackburn, H.M., Sherwin, S.J., Barkley, D.: Convective instability and transient growth in steady and pulsatile stenotic flows. J. Fluid Mech. **607**, 267–277 (2008)
6. Cantwell, C.D., Barkley, D., Blackburn, H.M.: Transient growth analysis of flow through a sudden expansion in a circular pipe. Submitted to Phys. Fluid.
7. Khalifa, A.M.A., Giddens, D.P.: Characterization and evolution of poststenotic disturbances. J. Biomech. **14**(5), 279–296 (1981)
8. Ojha, M., Cobbold, R.S.C., Johnston, K.W., Hummel, R.L.: Pulsatile flow through constricted tubes: an experimental investigation using photochromic tracer methods. J. Fluid Mech. **203**, 173–197 (1989)
9. Schmid, P.J., Henningson, D.S.: Optimal energy density growth in Hagen–Poiseuille flow. J. Fluid Mech. **277**, 197–225 (1994)
10. Schmid, P.J., Henningson, D.S.: Stability and Transition in Shear Flows. Springer, New York (2001)
11. Sexl, T., Über den von, E.G.: Richardson entdeckten 'annulareffekt' . Z. Phys. **61**, 349–362 (1930)
12. Sherwin, S.J., Blackburn, H.M.: Three-dimensional instabilities and transition of steady and pulsatile flows in an axisymmetric stenotic tube. J. Fluid Mech. **533**, 297–327 (2005)
13. Varghese, S.S., Frankel, S.H., Fischer, P.F.: Direct numerical simulation of stenotic flows. Part 1 Steady flow. J. Fluid Mech. **582**, 253–280 (2007)
14. Varghese, S.S., Frankel, S.H., Fischer, P.F.: Direct numerical simulation of stenotic flows. Part 2 Pulsatile flow. J. Fluid Mech. **582**, 281–315 (2007)
15. Womersley, J.R.: Method for the calculation of velocity, rate of flow and viscous drag in arteries when the pressure gradient is known. J. Physiol. **127**, 553–563 (1955)